

GT2018-75569

## LARGE EDDY SIMULATION OF BOUNDARY LAYER TRANSITION MECHANISMS IN A GAS-TURBINE COMPRESSOR CASCADE

Ashley D. Scillitoe<sup>1\*</sup>, Paul G. Tucker<sup>1</sup>, Paolo Adami<sup>2</sup>

<sup>1</sup>CFD Laboratory, Department of Engineering, University of Cambridge, Cambridge,  
CB2 1PZ, UK

<sup>2</sup>Core CFD Team Leader, CFD Methods, Rolls-Royce Deutschland, Eschenweg 11,  
15827 Blankenfelde-Mahlow, Germany

### ABSTRACT

*Large Eddy Simulation (LES) is used to explore the boundary layer transition mechanisms in two rectilinear compressor cascades. To reduce numerical dissipation, a novel locally adaptive smoothing scheme is added to an unstructured finite-volume solver. The performance of a number of Sub-Grid Scale (SGS) models is explored.*

*With the first cascade, numerical results at two different freestream turbulence intensities ( $Ti$ 's), 3.25% and 10%, are compared. At both  $Ti$ 's, time-averaged skin-friction and pressure coefficient distributions agree well with previous Direct Numerical Simulations (DNS). At  $Ti = 3.25\%$ , separation induced transition occurs on the suction surface, whilst it is bypassed on the pressure surface. The pressure surface transition is dominated by modes originating from the convection of Tollmien-Schlichting waves by Klebanoff streaks. However, they do not resemble a classical bypass transition. Instead, they display characteristics of the “overlap” and “inner” transition modes observed in the previous DNS. At  $Ti = 10\%$ , classical bypass transition occurs on both blade surfaces, with Klebanoff streaks resulting in the inception of turbulent spots.*

*With the second cascade, the influence of unsteady wakes on transition is examined. Wake-amplified Klebanoff streaks were found to instigate turbulent spots which periodically shorten the suction surface separation bubble. The 70% of free-stream celerity line, associated with the convection speed of the amplified Klebanoff streaks, was found to be important.*

### INTRODUCTION

In the low-pressure stages of a gas-turbine compressor, the Reynolds number is relatively low, and the flow may be transitional over a large portion of the blades [1]. This transitional behaviour can have a significant influence on the aerodynamic performance of the compressor.

Due to the reduced number of blades in modern aero-engine compressors the suction surface boundary layers are more prone to separation. The separated shear layer becomes turbulent soon after separation and quickly reattaches. The separation bubble alters the effective blade loading distribution, thus degrading the blade's performance. At higher free-stream turbulence intensities ( $Ti$ 's), earlier transition results in shorter separation bubbles [2]. However, the increased turbulent wetted area causes profile losses. Moreover, the transitional processes on the suction surface have been found to influence the deleterious corner separations that occur close to the endwalls [3], potentially leading to increased endwall losses. Additionally, wakes from upstream stages can also cause significant variations in the transition mechanisms and transition location in compressors. Adamczyk et al. [4] show that capturing these variations is vital to properly predicting the performance of a compressor stage.

In order for Computational Fluid Dynamics (CFD) to be effectively utilised to develop new compressor designs, it is important that the CFD tools can reliably predict the effects of free-stream turbulence and migrating wakes on transition, and therefore compressor performance. This is especially challenging, since the flow physics occurring in a compressor is complicated

---

\*Address all correspondence to this author (as2341@cam.ac.uk).

by the leading-edge and suction-side curvature, strong pressure gradients, and the complex nature of the turbulent flow through the passages. Laminar-to-turbulent transition can be triggered by impinging wakes, unstable Tollmien-Schlichting waves, background turbulence, or a combination of these [5]. When used with a transition model (e.g. [6]), Reynolds-Averaged Navier-Stokes (RANS) models are able to capture some of the first-order effects of transition. However, it is well known that they struggle to capture the more detailed physics, especially when there is not a spectral gap between the modelled and resolved unsteadiness.

An alternative CFD approach to RANS is Direct Numerical Simulation (DNS), where all the scales of turbulence are directly simulated. Zaki et al. [5] used DNS to study the interaction of grid-generated free-stream turbulence with the boundary layers in a compressor cascade. Although accurate, for the foreseeable future DNS is only suited to "one-off" simulations due to its extreme computational cost. Lardeau et al. [2] and Leggett et al. [7] have performed Large Eddy Simulations (LES) of the same case at a fraction of the cost. In both cases, good agreement was obtained with time-averaged quantities from the DNS of Zaki et al. [5]. However, it is less clear to what extent the LES captured the more detailed physics involved in the transition mechanisms. This paper aims to investigate this through the following two objectives:

1. The mechanisms of laminar-to-turbulent transition in a compressor cascade will be examined at two different free-stream Ti's. Comparisons will be made to the DNS of Zaki et al. [5] to determine if the same transition mechanisms are observed at both Ti's.
2. Wake induced transition will be simulated in a compressor cascade, to determine to what extent the observed physics matches that seen in previous experiments, such as the turbine cascade experiments of Coull and Hodson [30].

It is important to understand to what extent LES can capture the finer details of transition in compressors. This will provide confidence that LES may be used to further develop transition models and correlations for application in complex compressor flows.

## FLOW CONFIGURATIONS

The two linear compressor blade cascades detailed in Table 1 are simulated in this paper. Although not an up-to-date aerofoil profile, both aerofoil cascades have been used in many studies [8–11] to represent the compressor stator blades found in an axial flow gas-turbine compressor. Cascade 1 consists of NACA-65 aerofoils and was tested experimentally by Hilgenfeld and Pfitzner [11]. This cascade was also simulated at a lower  $Re_c$  using DNS by Zaki et al. [5] and using LES by Lardeau et al. [2]. Cascade 2 is a linear CDA (Controlled Diffusion Aerofoil) cascade investigated experimentally by Gbadebo et al. [10].

**TABLE 1:** Geometrical and inflow parameters for the two compressor cascades.

	Cascade 1	Cascade 2
Blade profile	NACA-65-k48	CDA
Chord length, $c$	220mm	151.5mm
Axial chord length, $C_x$	204mm	146.5mm
Reynolds number, $Re_c = U_1 c / \nu$	$1.38 \times 10^5$	$2.3 \times 10^5$
Aspect ratio	1.36	1.32
Inflow incidence	$-6.0^\circ$	$0.0^\circ$
Flow turning	$36.0^\circ$	$33.0^\circ$
2D Diffusion Factor [12]	0.42	0.49

To discretise each cascade a standard H-O-H mesh topology is used. For Cascade 1, a baseline mesh is designed to have a non-dimensional spacing of  $\Delta^+ < 50/1/15$  in the wall tangential/normal/spanwise directions at the wall. These grid resolutions are well within the recommended values for wall-resolved LES given by Piomelli and Chasnov [13]. The resulting O-block for this mesh has  $690 \times 45 \times 136$  points in the stream-wise/pitch-wise/span-wise directions, leading to a total of 9.3M grid points once the H-blocks are included. To check for mesh dependence, a finer mesh with double the number of stream-wise and span-wise grid points (37.4M in total) is also used for Cascade 1 (LES case C6 in Table 2).

The Cascade 2 mesh is designed to meet the same non-dimensional wall spacing limits as the baseline mesh for Cascade 1. Due to the higher Reynolds number of Cascade 2 the resulting number of grid points is higher, with 17.6M in total. More details of the meshes used can be found in Scillitoe et al. [3].

The blades are represented with no-slip walls, and standard velocity inlet and static pressure outlet boundaries are enforced. Downstream of the blade a sponge zone is used to prevent reflections from the outflow boundary. Pitchwise periodicity is enforced with periodic boundaries at mid-pitch. Following the DNS of Zaki et al., a span-wise extent of  $0.2C_x$  is used for all cases, with periodicity also enforced in this direction.

The LES cases run for Cascade 1 are listed in Table 2. A number of different cases are run to examine the influence of free-stream turbulence and the sensitivity to the SGS model. The free-stream turbulence intensities are chosen to match the DNS of Zaki et al. [5]. Two cases are run for Cascade 2, one with and one without incoming turbulent wakes, in order to examine their influence on the boundary layer transition. For both these cases, the free-stream Ti is set at 1.5% in order to match the experiments of Gbadebo et al. [10]. The incoming turbulent scales were not

**TABLE 2:** Cases simulated for Cascade 1.

Case	Inflow turbulence Ti (%)	$L/C_x$	SGS model	Mesh
C1	3.25	0.03	$\sigma$	Baseline
C2	3.25	0.06	$\sigma$	Baseline
C3	3.25	0.06	WALE	Baseline
C4	3.25	0.06	SM	Baseline
C5	10.0	0.06	$\sigma$	Baseline
C6	3.25	0.03	$\sigma$	Fine

measured in the experiment, therefore the integral length scale is arbitrarily set to  $L = 0.06C_x$  for Cascade 2.

## NUMERICAL METHOD

The code used is modified version of the Rolls-Royce CFD code HYDRA [14]. It is a second-order unstructured and finite-volume code, which has been successfully used for a number of low pressure turbine LES studies [15].

### Numerical Scheme

Originally, HYDRA solved the compressible Navier-Stokes equations. However, to improve the code's performance at low Mach numbers, it has been modified to use an artificial compressibility method [16]. This involves solving a modified form of the Navier-Stokes equations:

$$\frac{\partial D}{\partial \zeta} + \Gamma_t \frac{\partial D}{\partial t} + \frac{\partial}{\partial x_i} R(D) = 0 \quad (1)$$

where

$$D = \begin{Bmatrix} p \\ \rho u_1 \\ \rho u_2 \\ \rho u_3 \end{Bmatrix}, \quad R(D) = \begin{Bmatrix} \beta u_i \\ \rho u_1 u_i + p \delta_{i1} + 2\mu S_{1i} - \rho \bar{u}_1' \bar{u}'_{jSGS} \\ \rho u_2 u_i + p \delta_{i2} + 2\mu S_{2i} - \rho \bar{u}_2' \bar{u}'_{jSGS} \\ \rho u_3 u_i + p \delta_{i3} + 2\mu S_{3i} - \rho \bar{u}_3' \bar{u}'_{jSGS} \end{Bmatrix},$$

$\beta$  is the pseudo-compressibility constant,  $\zeta$  refers to pseudo-time,  $S_{ij} = 1/2(\partial u_i / \partial x_j + \partial u_j / \partial x_i)$  is the instantaneous strain rate tensor, and  $\Gamma_t = \text{diag}[0, 1, 1, 1]$ . Dual time stepping is used to advance the solution in real time. Second order backward-differencing is used to approximate the  $\partial D / \partial t$  term in Equation 1. During pseudo-time, a 3-stage Runge-Kutta scheme is used to drive the  $\partial D / \partial \zeta$  term towards zero, which ensure a divergence-free velocity field is satisfied. The density  $\rho$  and viscosity  $\mu$  are now user specified constants, chosen to give the desired Reynolds number.

HYDRA uses the Roe flux-differencing method [17] to solve for the inviscid flux through each control volume face. This is essentially central differencing, smoothed by some upwinding scaled by a smoothing constant  $\varepsilon_2$ :

$$F_{ij}^{I,S} = \underbrace{\frac{1}{2} (F_{ij}^I(Q_i) + F_{ij}^I(Q_j))}_{\text{Central differencing}} - \underbrace{\frac{1}{2} \varepsilon_2 |A_{ij}| (L_i^{lp} - L_j^{lp})}_{\text{Upwinding}} \quad (2)$$

$F_{ij}^I$  and  $F_{ij}^{I,S}$  are the original and smoothed inviscid fluxes through a cell face,  $|A_{ij}|$  is the flux Jacobian and  $L^{lp}$  is a Laplacian operator.

For eddy resolving simulations it is important to minimise the  $\varepsilon_2$  smoothing to prevent excessive numerical dissipation. However, reducing the smoothing too much results in dispersive errors, seen as wiggles in the solution. To avoid the need for manual tuning of the smoothing constant, some authors, such as Tajallipour et al. [18], propose Locally Adaptive Smoothing (LAS) schemes. Such schemes locally adapt the numerical smoothing across each  $e_{ij}$  edge, according to the local magnitude of any wiggle across the edge. Wiggle are said to be present if the following two conditions are met,

$$\begin{aligned} \theta_i(t) &= (\phi_i - \phi_{i-1})(\phi_j - \phi_i) < \theta_t < 0 \\ \theta_j(t) &= (\phi_{j+1} - \phi_j)(\phi_j - \phi_i) < \theta_t < 0 \end{aligned} \quad (3)$$

where  $\phi$  is the velocity or pressure, and  $\theta_t$  is the target wiggle magnitude (i.e.  $\theta_t = 0$ ). To adjust  $\varepsilon_2$ , Tajallipour et al. [18] propose using a proportional controller,  $\Delta\varepsilon_2(t) = [\theta_t - \min(\theta_i(t), \theta_j(t))] \alpha$ . However, preliminary tests on a forced isotropic turbulence test case [19] showed the controller to be overly sensitive to the gain parameter  $\alpha$ .

To improve the LAS scheme the LAS with windowing (LASW) procedure is introduced. The average wiggle magnitude is evaluated over the time window  $T_w$ ,

$$\theta_w = \frac{1}{T_w} \int_{t_w=0}^{t_w=T_w} \theta(t_w) dt_w \quad (4)$$

where  $\theta = \sqrt{|\max(\theta_i(t), \theta_j(t))|}$  is the wiggle magnitude. The proportional controller,  $\Delta\varepsilon_2(t) = (\theta_w(t) - \theta_t) \alpha$ , is only applied when  $t_w \geq T_w$ . Then,  $t_w$  and  $\theta_w$  are zeroed ready for the next window. Windowing provides a less intermittent error signal for the proportional controller, and avoids the increasing insensitivity to the error signal that an integral controller would suffer from. As long as  $T_w$  is large enough, the  $\varepsilon_2$  field was found to converge to a steady state, independent of the gain parameter  $\alpha$ . The resulting  $\varepsilon_2$  field for LES case C1 is shown in Figure 1. Low dissipation central differencing is used in most of the domain, with small

amounts of numerical smoothing added where necessary to prevent wiggles. The LASW scheme is used for all the simulations described in this paper, with  $T_w = 0.2T^*$ ,  $\alpha = 1.0$ , and  $\theta_t = 0.0$ .

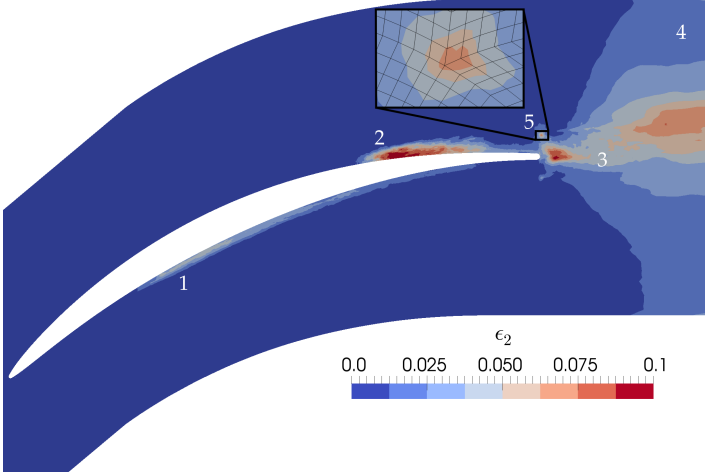


**FIGURE 1:** Contours of converged  $\epsilon_2$  smoothing field with LASW scheme, for Case C1.

### Sub-Grid Scale Modelling

The modelled (unresolved) stresses in Equation 1 are obtained via the Boussinesq approximation:

$$-\rho \bar{u}_i' \bar{u}_j'_{SGS} = 2\mu_{sgs} \left( S_{ij} - \frac{1}{3} S_{kk} \delta_{ij} \right). \quad (5)$$

where the SGS viscosity  $\mu_{sgs}$  is given by a Sub-Grid Scale (SGS) model. A number of SGS models are used in this paper, the first is the Smagorinsky-Lilly (SM) model [20], which defines the SGS viscosity as:

$$\mu_{sgs} = \rho \Delta_{sgs}^2 \sqrt{2S_{ij}S_{ij}} \quad (6)$$

To prevent high aspect ratio cells near walls leading to excessively high  $\mu_{sgs}$  values, Schumann's near-wall limiter [21],  $\Delta_{sgs} = \min(C_s \Delta_{vol}, \kappa d)$ , is used.

The second SGS model used is the Wall-Adapting-Local-Eddy-viscosity (WALE) model introduced by Nicoud and Ducros [22]:

$$\mu_{sgs} = \rho (C_w \Delta_{vol})^2 \frac{(S_{ij}^d S_{ij}^d)^{3/2}}{(S_{ij} S_{ij})^{5/2} + (S_{ij}^d S_{ij}^d)^{5/4}} \quad (7)$$

The  $S_{ij}^d S_{ij}^d$  term is based on both strain and vorticity and is formulated to give zero SGS viscosity in pure shear regions such as a laminar boundary layer.

The final model tested is the  $\sigma$  model also proposed by Nicoud et al. [23], which bases the SGS viscosity on the singular values ( $\sigma_1, \sigma_2, \sigma_3$ ) of the resolved gradient tensor:

$$\mu_{sgs} = \rho (C_\sigma \Delta_{vol})^2 \frac{\sigma_3(\sigma_1 - \sigma_2)(\sigma_2 - \sigma_3)}{\sigma_1} \quad (8)$$

The WALE and  $\sigma$  model constants recommended by Nicoud et al. [22, 23] ( $C_w = 0.5$  and  $C_\sigma = 1.35$ ) are used. For isotropic decaying turbulence these constants give dissipation equal to using the Smagorinsky model with  $C_s \approx 0.165$ , therefore this value is chosen for the Smagorinsky model here.

### Time Dependent Inflow Conditions

To represent free-stream turbulence (FST), isotropic turbulence generated using an open-source synthetic turbulence tool [24] is added onto the mean inflow velocity boundary condition. The tool generates a divergence-free velocity field that matches a given energy spectrum, in this case the von Kármán-Pao spectrum:

$$E(\kappa) = \alpha \frac{u'^2}{\kappa_e} \frac{(\kappa/\kappa_e)^4}{[1 + (\kappa/\kappa_e)]^{17/6}} \exp \left[ -2 \left( \frac{\kappa}{\kappa_\eta} \right)^2 \right] \quad (9)$$

where  $u'$  is the RMS value of the velocity fluctuations,  $\kappa_e$  is related to the wavenumber of maximum energy ( $\kappa_p = \sqrt{12/5} \kappa_e$ ), and  $\kappa_\eta = \varepsilon^{1/4} v^{-3/4}$  is the Kolmogorov wave number. As recommended by Bailly and Juve [25] for isotropic turbulence,  $\alpha = 1.453$ , and  $\varepsilon = u'^3/L$  with  $L$  being the integral length scale  $L = 0.746834/\kappa_e$ .

The turbulent wake data is obtained from a separate simulation [26], which has been kindly provided by Dr. Xiaohua Wu. This data was generated by initially fusing two half-channel flow simulations ( $Re_b = 3300$ ) and allowing the solution to develop until it reaches a statistically steady state.

Wake parameter	Value
Mean velocity deficit	$0.2U_0$
Half-width	$0.05C_x$
Vertical separation	$0.9P$ ( $P$ is blade pitch)
Cycle velocity	$0.8U_1$
Wake passing period, $\tau_w$	$1.09C_x/U_1$
Reduced frequency, $f_r = \frac{1}{\tau_w} \frac{C_x}{U_{TE}}$	1.2

**TABLE 3:** Parameters of incoming turbulent wake.

The wake data is scaled by the parameters given in Table 3.

These values are chosen so that the incoming wakes are representative of those seen by stator stages in a gas turbine engine. The wake data is applied to the inflow using the procedure given in Wu et al. [26].

### Simulation Time/Cost

The time-step is set to give  $CFL_{max} \approx 0.8$ , and a flow-through time ( $T^*$ ) equates to approximately 10000 time-steps. The simulations without wakes were run for  $4T^*$  to clear the initial transients, then a further  $10T^*$  to collect statistics. The simulation with wakes present was run for 6 wake passing periods ( $\tau = 1.09T^*$ ) to establish a periodic flow, followed by  $28\tau$  to obtain well converged phase averages. All time and phase-averaged data is also averaged in the span-wise direction.

All simulations were run on 128 to 512 processing cores on ARCHER, the UK's National HPC facility. ARCHER is a Cray XC30 MPP supercomputer consisting of 4920 compute nodes, each with two 12-core Intel Ivy Bridge Processors. Simulations required 1-2 kCPU hours per  $T^*$ .

### INFLUENCE OF FREE-STREAM TURBULENCE INTENSITY ON THE TRANSITION MECHANISMS

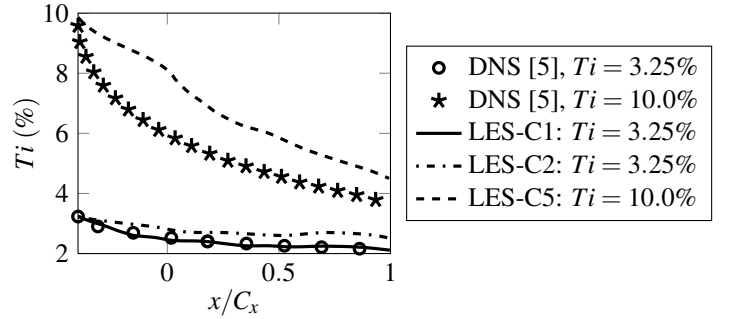
For the majority of the cases in Table 2 the integral length scale of the free-stream turbulence was chosen as  $L = 0.06C_x$  in order to match the DNS [5]. The turbulence intensity is defined as  $Ti = \sqrt{u'_i u'_i} / 3U_1^2$ , where  $U_1$  is the inflow bulk velocity, and fluctuating quantities are obtained through the standard Reynolds decomposition,  $f' = \bar{f} - f$ .  $Ti$  at mid-pitch in a number of LES cases is compared to the DNS in Figure 2. It was found that  $L = 0.06C_x$  resulted in a slower decay rate of  $Ti$  compared to the DNS. This may be due to differences in the definition of the integral length scale used by Zaki et al. [5] and that used in the synthetic turbulence method of Saad et al. [24], or due to differences in the energy spectra of the FST.

To enable a fair comparison with the DNS, one additional case (C1) was run with a smaller inflow integral length scale  $L = 0.03C_x$ . Figure 2 shows that the FST decay rate is in much closer agreement with the DNS in this case. Despite the lower FST decay rate in the other cases, a comparison of cases C1 and C5 still provides a valid basis to examine the influence of free-stream turbulence on the transition mechanisms.

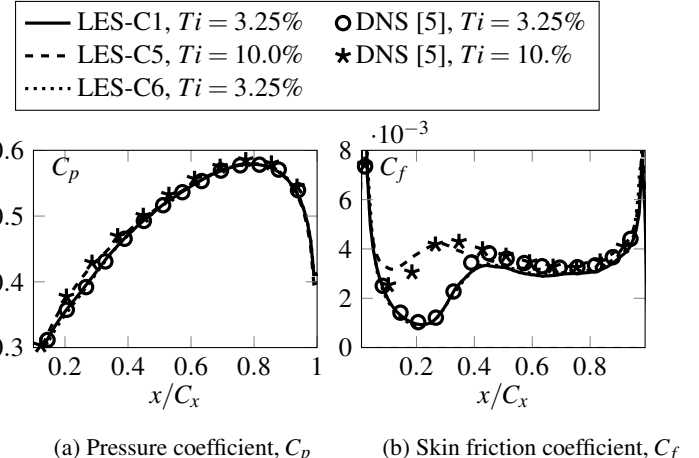
### Pressure Surface Transition Mechanisms - Moderate Free-Stream Turbulence Intensity

Figure 3 shows the pressure surface distributions of the time averaged pressure coefficient,  $C_p = (\bar{p} - \bar{p}_1) / (\frac{1}{2}\rho U_1^2)$ , and the time-averaged skin friction coefficient,  $C_f = \tau_w / (\frac{1}{2}\rho U_1^2)$ .  $\tau_w$  is the wall shear stress and  $\bar{p}_1$  is the time averaged static pressure at the inflow.

From the  $C_p$  distribution in Figure 3a, it is clear that the FST has some effect, and this becomes more apparent in the  $C_f$  distri-



**FIGURE 2:** Turbulence intensity,  $Ti$ , at mid-pitch of Cascade 1.



**FIGURE 3:** Time-averaged pressure and skin friction coefficients on the pressure surface of cascade 1.

bution in Figure 3b. In the absence of free-stream perturbations, the suction surface flow separates (indicated by  $C_f \leq 0$ ) in the laminar ( $Ti = 0\%$  case) DNS case of Zaki et al. [5]. On the other hand, in the present cases where free-stream perturbations are present, the boundary layer is transitioned to turbulence and the flow is prevented from separating.

Despite the slightly premature transition in the  $Ti = 10.0\%$  case (due to the slower decay of the incoming FST, seen in Figure 2), the effect of FST on the time-averaged flow is generally well captured by the LES. However, as discussed in the introduction, breakdown to turbulence in turbo-machinery flows can be caused by a number of different mechanisms. In the following sections the pressure surface transition mechanisms are examined in more detail to see if the finer physics is properly captured by the LES. Cases C6 and C1 are in close agreement in Figure 3, suggesting that a satisfactory level of grid independence is reached with the baseline mesh for Cascade 1.

In Figure 4 the pressure surface transition process under moderate FST (Case C1,  $Ti = 3.25$ ) is visualised using iso-surfaces of Q-criterion. The locations of transition onset ( $X_s$ )

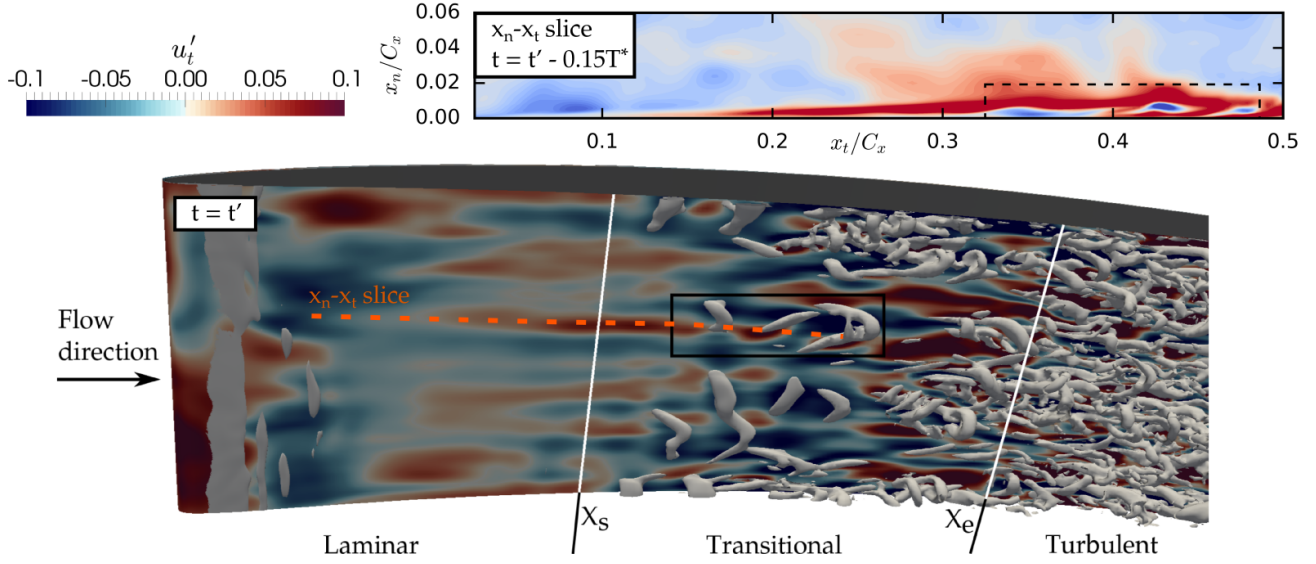


**FIGURE 4:** Contours of the tangential velocity perturbations on a plane inside the pressure surface boundary layer,  $d^+ \approx 15$  from the wall. An iso-surface of  $Q = 200U_0/C_x$  is superimposed. Also shown is an  $x_n - x_t$  slice bisecting the  $\Lambda$ -structure, at a time instance  $0.15T^*$  prior to the main image.

and completion ( $X_e$ ) are shown by the white lines. Following Zaki et al. [5],  $X_s$  is defined as the minimum  $C_f$  location in Figure 3b, while  $X_e$  is the point where  $C_f$  plateaus. Figure 4 shows contours of the tangential velocity perturbations,  $u'_t = u'_x + v'_y$ , at  $d^+ \approx 15$  from the wall.  $(t_x, t_y)$  is the two-dimensional streamwise unit tangent, and  $d^+ = d\sqrt{\tau/\rho}/\mu$  is the non-dimensional wall distance. These contours show that in the laminar region ( $x < X_s$ ), the boundary layer is dominated by streaks of strong forward and backward tangential velocity. To determine whether these streaks are related to Görtler instabilities the Görtler number,  $G \equiv \sqrt{\theta/R}(\bar{u}_e\theta/v)$ , is plotted in Figure 5. Here,  $R$  is the local radius of curvature of the wall,  $\theta$  is the boundary layer momentum thickness, and  $U_e$  is the edge of boundary layer velocity. Saric [27] found that the boundary layer on a concave surface becomes unstable at  $G \sim 0.3$ , but Görtler vortices are not detected until  $G \sim 5 - 6$ . Figure 5 shows that  $G > 5$  for only a very small streamwise distance before transition, and thus Görtler vortices are not likely to occur. Zaki et al. [5] also failed to detect Görtler vortices, and instead showed that these streaks are Klebanoff distortions forced by the low-frequency component of the FST.

The natural transition of boundary layers via Tollmien-Schlichting (TS) waves is often bypassed when  $Ti > 1\%$  [28]. However, Zaki et al. [5] found that at  $Ti = 3.25\%$ , the instability modes observed on the pressure surface do not resemble the traditional bypass mechanism. Instead, two distinct near-wall modes were found. These modes were also observed in the present LES case, and are visualised in Figure 6. Although these modes are not streak instabilities, as the following two sections will show, they are influenced by the Klebanoff streaks. In both modes, vortical structures develop in (or slightly upstream of) the

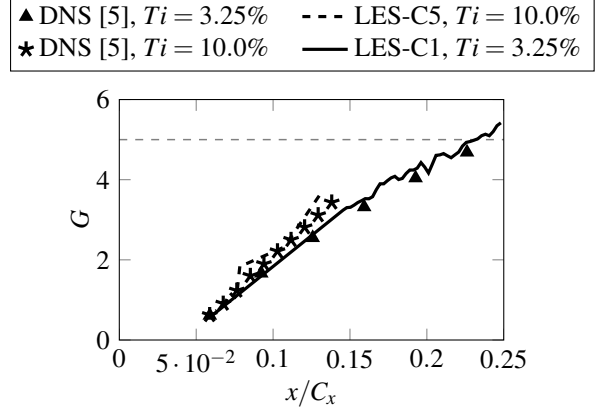


**FIGURE 5:** Görtler number,  $G$ , (upstream of transition/separation) on the pressure surface.

transitional region ( $X_s < x < X_e$ ), and then breakdown to turbulence.

**The inner mode** The so-called *inner mode* structure shown in Figure 6a is also highlighted by the black box in Figure 4. These strong vortices are referred to as  $\Lambda$ -vortices due to their shape. Their presence hints at a natural transition mechanism. However, as noted by Zaki et al. [5], they can not be independent of the streaks as they would then be observed homogeneously across the blade span. The structures span-wise size is not directly related to the streaks; in LES case C1 the average span-wise wavelength of the streaks is approximately  $0.015C_x$ , but the  $\Lambda$  structures' width ranges from  $0.02C_x$  to  $0.035C_x$ .

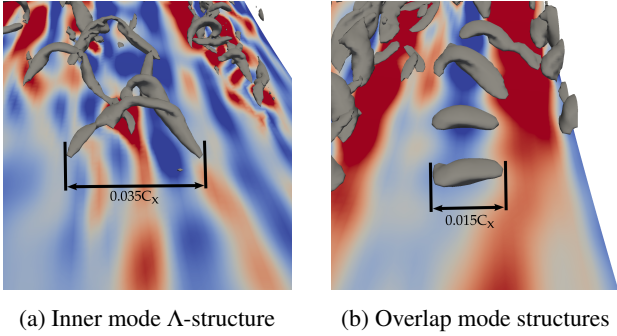


**FIGURE 6:** Two of the vortical structures present on the pressure surface, visualised using iso-surfaces of  $Q = 200U_0/C_x$ . Contours of  $-0.1 < u'_t < 0.1$  are also shown.

Figure 4 also shows the  $u'_t$  field on a wall tangential-normal ( $x_t - x_n$ ) plane bisecting the  $\Lambda$ -structure, at a time  $0.15T^*$  prior to that in the main image. The disturbance (highlighted by the black dashed box) is initiated below the forward-velocity streak, hence the name “inner” mode. Very similar behaviour is observed in the DNS [5].

**The overlap mode** The second mode observed is the overlap mode, shown in Figure 6b. This mode is also an inner instability. However, it is characterised by a significantly shorter span-wise wavelength than the inner mode. Here, the instability has the same width as the host streak.

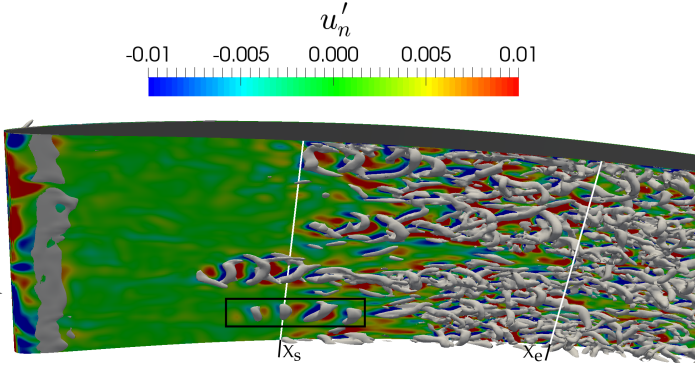


**FIGURE 7:** Contours of the normal velocity perturbations,  $u'_n$ , on the  $d^+ \approx 15$  pressure surface plane. An iso-surface of  $Q = 200U_0/C_x$  is superimposed.

The inception of these instabilities can be easily observed by examining contours of wall-normal velocity fluctuations ( $u'_n = -u't_y + v't_x$ ), like those in Figure 7. The instability typically starts some distance upstream of  $X_s$ . The  $x_n - x_t$  slice in Figure 8 shows that the instabilities are located where the downstream edge of a high speed streak overlaps with the upstream edge of a low speed streak. Again, this behaviour is in agree-

ment with the DNS results of Zaki et al. [5].

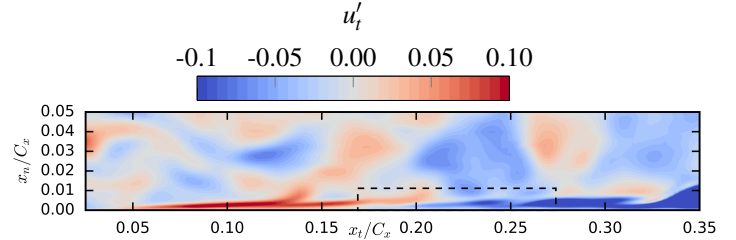


**FIGURE 8:** Contours of the tangential velocity perturbations,  $u'_t$ , on an  $x_t - x_n$  plane bisecting the overlap mode structure highlighted in Figure 7. The time is  $0.1T^*$  prior to that in Figure 7.

### Suction Surface Transition Mechanisms - Moderate Free-Stream Turbulence Intensity

The suction surface  $C_p$  and  $C_f$  distributions are plotted in Figure 9. Generally, like for the pressure surface, the overall effect of  $Ti$  is well captured by the LES. Again, cases C6 and C1 are in close agreement, suggesting that a satisfactory level of grid independence is reached with the baseline mesh. Unlike on the pressure surface, the flow separates on in the  $Ti = 3.25\%$  case here.

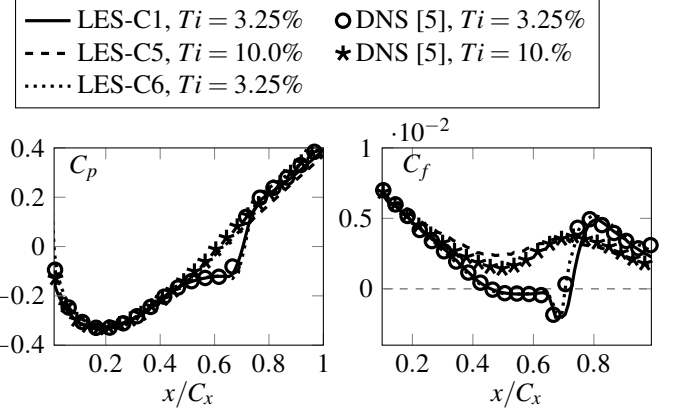


**FIGURE 9:** Pressure and skin friction coefficients on the suction surface of Cascade 1.

In Figure 10 the suction surface in LES case C1 ( $Ti = 3.25$ ) is displayed. Similarly to the pressure surface, a streaky laminar region is visible. The laminar boundary layer undergoes separation in the adverse pressure gradient region close to the time-averaged separation location  $x_s$ , and Kelvin-Helmholtz (K-H) rolls develop. Transition has still not occurred at  $x_s = 0.46$ , which is significantly downstream from the pressure surface transition location ( $X_s = 0.22$ ). This is explained by the fact that Kle-

banoff streaks, a precursor for transition here, are found to amplify faster in the presence of an adverse pressure gradient [29].

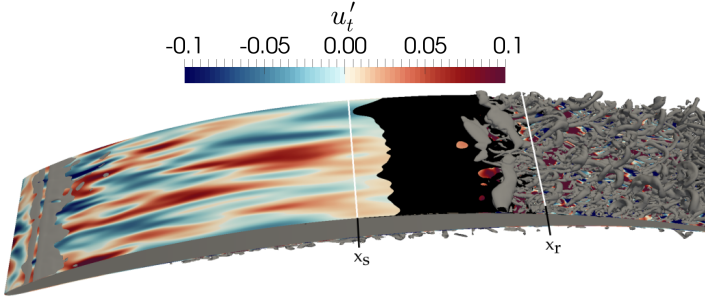


**FIGURE 10:** Contours of the tangential velocity perturbations,  $u_t'$ , on a plane inside the suction surface boundary layer  $d^+ \approx 15$  from the wall. Iso-surfaces of  $Q = 300U_0/C_x$  (grey) and  $u_t < 0$  (black) are superimposed.

In the laminar DNS case [5], the K-H rolls remain laminar and convect downstream, maintaining a separation region in their shadow. However, in the  $Ti = 3.25\%$  DNS case, the K-H rolls are quickly destabilized by the free-stream turbulence. The rolls break down and are followed by turbulent reattachment of the boundary layer. This process is well captured by the LES; with an attached turbulent boundary layer visible after  $x_r$  in Figure 10, and the LES  $C_f$  agreeing well with the DNS at  $x \geq 0.72$  in Figure 9b.

The time averaged  $C_f$  profile in Figure 9b suggests that a free-stream  $Ti$  of  $3.25\%$  has little influence on the separation location. However, the instantaneous separation region shown by the black iso-surface in Figure 10 shows that the separation location varies in time. This is due to the Klebanoff streaks; separation is shifted upstream where elongated  $u_t'$  contours are negative, and downstream where they are positive. This effect is well captured by the LES, with the resulting K-H rolls seen to be more three-dimensional than in the laminar DNS case of Zaki et al. [5].

### Transition Mechanisms at High Free-Stream Turbulence Intensity

At the higher free-stream  $Ti$  of  $10\%$ , a streaky laminar boundary layer is still present upstream of transition on both surfaces. But, the strength of the streaks is increased from  $\approx \pm 0.1U_1$  in the  $Ti = 3.25\%$  case (e.g. see Fig. 4), to  $\approx \pm 0.2U_1$ . The transition on both surfaces now occurs via the classical bypass transition mode characterised by Jacobs et al. [28]. Here, the strong negative velocity Klebanoff streaks are lifted towards the top of the boundary layer, where they are exposed to the free-stream turbulence. The interaction here is unstable and results in a turbulent spot forming, like the one seen in Figure 11. This is convected downstream, and eventually breaks down forming a fully turbulent boundary layer.

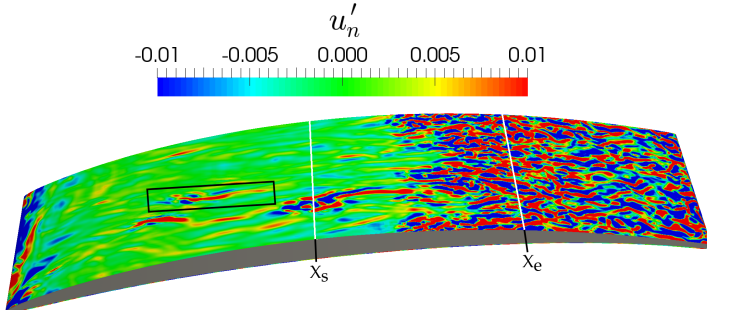


**FIGURE 11:** Contours of the normal velocity perturbations,  $u_n'$ , on a plane inside the suction surface boundary layer  $d^+ \approx 15$  from the wall. The time is the same as that in Figure 10.

On the pressure surface, this mechanism causes the inner and overlap transition modes to be bypassed, and the transition point moves upstream from  $X_s = 0.22C_x$  with  $Ti = 3.25\%$  to  $X_s = 0.13C_x$  with  $Ti = 10\%$ , as seen in Figure 3. On the suction surface, Figure 9 shows there is little change in  $C_f$  in the favourable pressure gradient region, but  $C_f$  remains higher in the adverse pressure gradient region compared to in the  $Ti = 3.25$  case. This higher  $C_f$  prevents the boundary layer from separating.

### SENSITIVITY TO THE SGS MODEL

In a previous paper by the authors [3], the sensitivity to the SGS models was examined. In the present section, a more in depth study on the effect of the different SGS models is presented. In Figure 12 the  $C_f$  distributions for cases C2, C3 and C4 are plotted, along with the LES results of Lardeau et al. [2]. The WALE and  $\sigma$  SGS model predictions are seen to compete well with the Dynamic Smagorinsky (DSM) SGS model predictions of Lardeau et al. [2].

On the other hand, the Smagorinsky-Lilly (SM) model performs poorly on both surfaces. On the pressure surface, the inner and overlap instabilities occur much later, suggesting the excessive SGS viscosity is damping them. On the suction surface, the boundary layer separates earlier, leading to a significantly larger separation bubble. Figure 13a shows the boundary layer velocity profiles at  $x = 0.4C_x$ . The boundary layer is noticeably thicker in case C4, with a smaller near-wall gradient, meaning it is less able to resist the adverse pressure gradient. Figure 13b shows profiles of the term  $u_n' \partial u_t / \partial x_n$ , which contributes to the production of turbulent shear stress  $u_t' u_n'$ . High free-stream forcing in the  $Ti = 10\%$  case (C5) leads to significantly increased  $u_n' \partial u_t / \partial x_n$  in the suction surface boundary layer. The resulting shear-stress leads to greater momentum transport inside the boundary layer, producing a less separation prone boundary layer. However, for cases C2 and C4, the  $\overline{u_t' u_n'}$  profiles in Figure 13b are in close agreement. This suggests that the above mechanism discussed for the  $Ti = 10\%$  case is not the cause of the inaccurate velocity

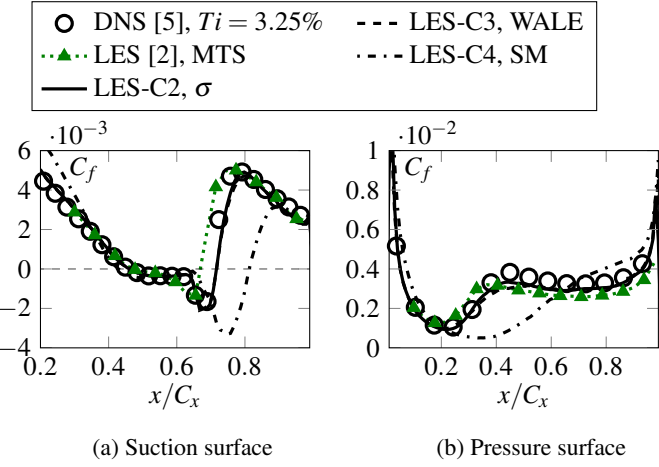


**FIGURE 12:** Skin friction coefficient distributions for Cascade 1 with inflow  $Ti = 3.25\%$ , with various SGS models used.

profile for the SM model case (C4) seen in Figure 13a.

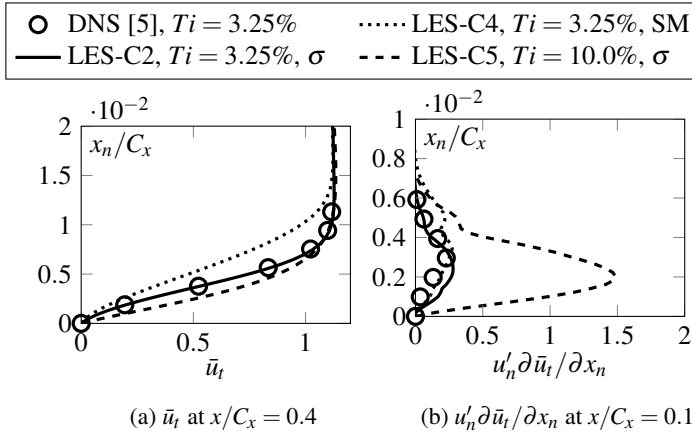


**FIGURE 13:** Profiles of  $u'_n \partial \bar{u}_t / \partial x_n$  and  $\bar{u}_t$  on the suction surface.

A more obvious difference between the two SGS models is seen when the turbulent tangential ( $\bar{u}'_t \bar{u}'_t$ ) and shear ( $\bar{u}'_t \bar{u}'_n$ ) stress profiles are separated into resolved and modelled/SGS (see eqn. 5) contributions in Figure 14. The shear stress in the laminar boundary layer in the SM model case (Fig. 14a) is much larger than in the  $\sigma$  model case (Fig 14b), and the absence of a green shaded region here indicates this is almost entirely due to the contribution from the SM model. This additional shear stress would be expected to cause additional momentum transfer in the boundary layer, and it seems plausible that it is this term causing the large discrepancy in the suction surface predictions of cases C2 and C4.

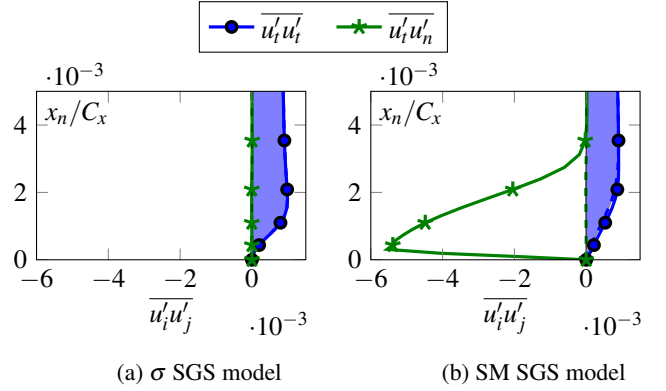


**FIGURE 14:** Profiles of the tangential ( $\bar{u}'_t \bar{u}'_t$ ) and shear ( $\bar{u}'_t \bar{u}'_n$ ) components of the Reynolds stresses on the suction surface at  $x/C_x = 0.025$ . Solid lines show the total ( $\bar{u}'_t \bar{u}'_j = \bar{u}'_t \bar{u}'_{j,SGS} + \bar{u}'_t \bar{u}'_{j,r}$ ) stresses, filled areas show only the resolved stresses ( $\bar{u}'_t \bar{u}'_{j,r}$ ).

## EFFECT OF UNSTEADY TURBULENT WAKES

In this section, the effect of unsteady turbulent wakes on Cascade 2 is examined. The free-stream turbulence is slightly lower at  $Ti = 1.5\%$ . Without wakes, the same transition mechanisms are observed; the inner and overlap instabilities occur on the pressure surface, whilst on the suction surface there is separation induced transition.

Since

The influence of the wakes can be elucidated by obtaining averaged quantities at a particular phase,  $0 \leq \phi \leq 1$ , of the wake passing period,

$$\langle f \rangle (\phi) = \frac{1}{N} \sum_{n=1}^N f(t = \phi \tau + n \tau) \quad (10)$$

where  $\langle \cdot \rangle$  denotes a phase-averaged quantity,  $\tau$  is the wake passing period, and  $N = 28$  is the total number of wake passing periods. Phase-averaged skin friction distributions are plotted in Figure 15. On the suction surface, the skin friction distribution is seen to vary significantly as the wake passes. On the other hand, Figure 15b suggests that the pressure surface transition mechanisms are not significantly influenced by the passing wakes.

The phase dependent variation of  $\langle C_f \rangle (\phi)$  on the suction surface can be seen more clearly in a phase-averaged space-time (ST) plot, presented in Figure 16. The separation bubble region is identified by the region of negative  $\langle C_f \rangle (\phi)$  (blue region), and it is bounded by the separation and reattachment lines (dashed blue lines), identified by  $\langle C_f \rangle (\phi) = 0$ . Throughout the wake passing period, the separation and reattachment points of the laminar separation bubble (dashed blue lines) are seen to move away from the time-averaged locations in the case without wakes (dashed grey lines). As a result, the bubble length fluctuates from a maxi-

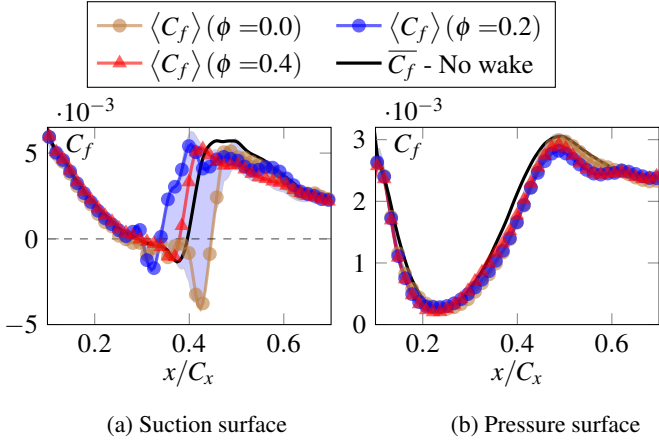


**FIGURE 15:** Phase-averaged and time-averaged skin friction coefficient distributions for Cascade 2. The filled area shows the range of  $\langle C_f \rangle (\phi)$  variation throughout the wake passing period.

mum of  $0.177C_x$  to a minimum of  $0.043C_x$ , compared to a length of  $0.105C_x$  in the case without wakes. Figure 16 shows that the centre of the wake passes  $x = 0.44C_x$  at  $\phi = 0.88$ , but the reattachment point isn't brought forward until  $\phi = 1.01$ . To explain this lag, celerity lines of  $0.5U_{fs}$ ,  $0.7U_{fs}$ ,  $0.88U_{fs}$  are overlaid.  $U_{fs}$  is taken as the free-stream (edge of time-averaged boundary layer) velocity magnitude, with the edge of the boundary layer detected using a vorticity magnitude threshold [2, 15]. The celerity lines are positioned to originate from where the phase-averaged  $C_f$  indicates the first appearance of turbulent disturbances ( $x = 0.06C_x$ ). The  $0.88U_{fs}$  and  $0.5U_{fs}$  celerity lines are important because these are the approximate convection rates of a turbulent spot leading and trailing edge [30]. Coull and Hodson [30] showed that the strongest wake induced disturbances on a turbine blade, which they demonstrated are amplified Klebanoff streaks, also convect at this speed.

The early reattachment induced by the wake is bounded by the  $0.5U_{fs}$  and  $0.7U_{fs}$  celerity lines. This suggests that wake induced disturbances, originating from near the leading edge, convect at approximately  $0.7U_{fs}$ . Once they reach the separation region, they initiate earlier transition in the K-H rolls, leading to earlier reattachment. This process is visualised in Figure 17. At  $\phi = 0.6$  in Figure 17a, amplified Klebanoff streaks have been induced by the passing wake, but they are lagging some distance behind due to their slower convection speed. In Figure 17b, these amplified Klebanoff streaks are seen to initiate a turbulent spot, via the negative velocity streak lift-off mechanism discussed previously. This spot continues to grow as it convects downstream, and eventually causes the K-H rolls to transition earlier, leading to the reattachment point moving upstream.

Figure 16 shows that, after the trailing edge of the wake-amplified Klebanoff streaks (travelling at  $0.5U_{fs}$ ) have convected past, a relatively slow drop in shear stress occurs. Eventually, the

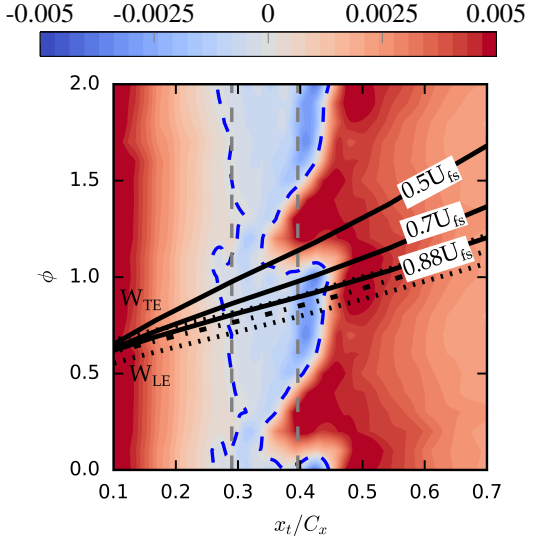


**FIGURE 16:** Phase-averaged space-time plots of the suction surface boundary layer skin friction coefficient  $C_f$ . The dashed blue lines indicate the phase dependent separation/reattachment locations (indicated by  $\langle C_f \rangle (\phi) = 0$ ). For clarity the range  $0 \leq \phi \leq 1$  is repeated to  $1 \leq \phi \leq 2$ .

reattachment line moves downstream of its wake-free location. This is characteristic of the calmed region that has been found to follow turbulent spots [31].

## CONCLUSIONS

The following conclusions are drawn from this study:

- With the proposed Locally Adaptive Smoothing with Windowing (LASW) scheme, and a suitable SGS model, LES is able to give predictions that are in good agreement with DNS. The LASW scheme minimised the numerical dissipation while preventing dispersive errors, avoiding the need for manual tuning with reference to a priori data.
- In addition to giving good mean flow predictions, the LES has been found to accurately capture the complex transition mechanisms. The inner and overlap modes, observed by Zaki et al. [5], were well replicated by the LES. Although still influenced by the Klebanoff streaks, these modes don't resemble the traditional mechanism observed in DNS of bypass transition [28]. The sensitivity to free-stream turbulence intensity is also well captured.
- Despite studies reporting the poor performance of the Smagorinsky-Lilly SGS model in transitional flows [32], it is still commonly used. The present study confirmed that the model is unsuitable for these flows. The excessive SGS viscosity in the laminar boundary layers leads to premature separation on the suction surface, and it damps the inner and

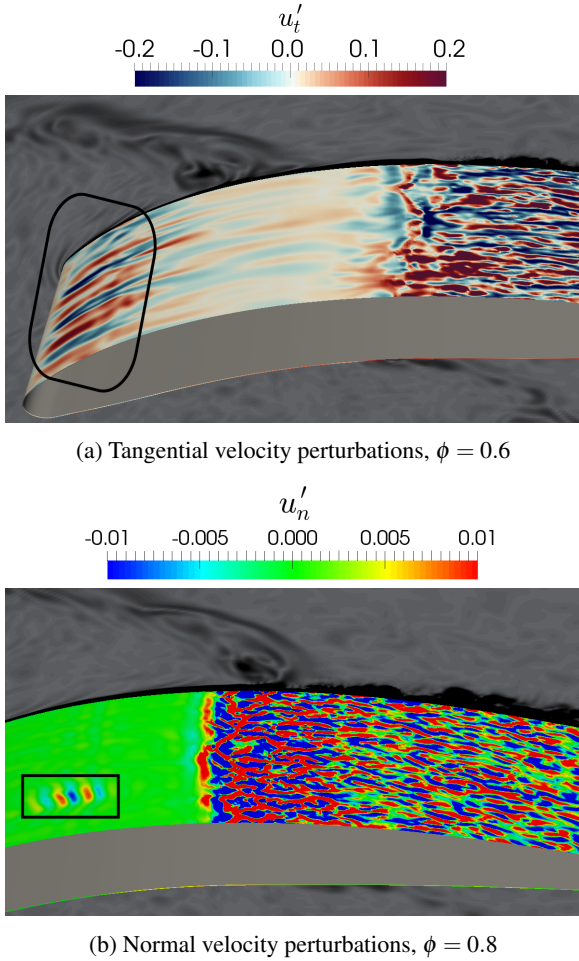


**FIGURE 17:** Contours of the tangential and normal velocity perturbations ( $f'(\phi) = f - \langle f \rangle(\phi)$ ) on the suction surface  $d^+ \approx 15$  plane. To show the passing wake, contours of instantaneous vorticity magnitude are shown at  $z = 0$  (greyscale).

overlap instabilities on the pressure surface. Encouragingly, the WALE and Sigma models perform much better here, and offer a promising alternative to more involved models such as the Dynamic Smagorinsky approach.

4. Incoming turbulent wakes amplified Klebanoff streaks in the laminar boundary layers. The streaks were found to instigate turbulent spots, which periodically shorten the suction surface separation bubble. The 70% of free-stream celerity line, associated with the convection speed of the amplified Klebanoff streaks, was found to be important here. This has similarities with the wake induced transition mechanism in turbine flows, reported by Coull and Hodson [30].

## ACKNOWLEDGMENT

This work was supported by the EPSRC through an iCASE award sponsored by Rolls-Royce plc. Rolls-Royce plc are gratefully acknowledged for allowing the use and modification of their CFD solver HYDRA. The work used the ARCHER UK National Supercomputing Service (<http://www.archer.ac.uk>) under EPSRC grant EP/L000261/1, and thanks go to both for their support. Finally, the authors would like to thank Dr. Ifthekar Naqavi, Dr. Rob Watson, Mr. Jiahuan Cui and Mr Bryn Ubald for their invaluable inputs, and Dr. Tamer Zaki for providing the geometry for cascade 1.

## NOMENCLATURE

$x, y, z$	Axial, pitch-wise, span-wise co-ordinates
$Re_{\square}$	Reynolds number, $Re = \frac{U_{\square}}{v}$ , based on the length-scale $\square$
$c$	Blade chord
$C_x$	Blade Axial chord
$C_p$	Static pressure coefficient, $(p - p_1)/(\frac{1}{2}\rho U_1^2)$
$C_f$	Skin friction coefficient, $\tau_w/(\frac{1}{2}\rho U_1^2)$
$d$	Wall distance
$\mu$	Dynamic viscosity
$\varepsilon_2$	Smoothing constant for the Roe scheme
$\theta$	Wiggle magnitude
$\theta_t$	Target wiggle magnitude
$\theta_w$	Window averaged wiggle magnitude
$\kappa$	Wave number
$v$	Kinematic viscosity, $v = \mu/\rho$
$\rho$	Density
$\tau_w$	Wake passing period, or wall shear stress
$\phi$	Any primitive variable or phase of wake passing period
$C_{s,w,\sigma}$	Constant Smagorinsky/WALE/Sigma SGS models
$L$	Turbulent integral length-scale
$p$	Static pressure
$S_{ij}$	Rate-of-Strain tensor, $S_{ij} = (\partial u_i / \partial x_j + \partial u_j / \partial x_i)$
$t_w$	Time through LASW scheme's window
$T_w$	LASW scheme's window length
$T^*$	Flow-through time
$u, v, w$	Velocity components in the x,y,z directions
$U$	Magnitude of velocity, $U = \sqrt{u^2 + v^2 + w^2}$
$X_s/X_e$	Start/end of transition region
$x_s/x_r$	Time-averaged separation/reattachment location
$x_t/x_n/z$	Coordinate system tangential/normal/span-wise to blade surface

## Subscripts and superscripts

$+$	Non-dimensional distance, given by $\square^+ = \frac{\square}{\sqrt{\tau_w/\rho}}$
$1$	Inflow quantity
$2$	Outflow quantity
$e$	Edge of boundary layer quantity
$FS$	Free-stream quantity
$TE$	Trailing edge quantity

- r* Contribution from resolved fluctuations  
*sgs* Contribution from SGS model

## Abbreviations

CDA	Controlled Diffusion Aerofoil
CFD	Computational Fluid Dynamics
CFL	Courant Friedrichs Lewy condition
DNS	Direct Numerical Simulation
FST	Free-Stream Turbulence
K-H	Kelvin-Helmholtz
LAS(W)	Locally Adaptive Smoothing (with Windowing)
LES	Large Eddy Simulation
MTS	Mixed Time-Scale
RANS	Reynolds Averaged Navier-Stokes
SGS	Sub-Grid Scale
SM	Smagorinsky-Lilly Model
Ti	Turbulence intensity (usually free-stream)
T-S	Tollmien-Schlichting
WALE	Wall-Adapting-Local-Eddy viscosity model

## REFERENCES

- [1] Steinert, W., and Starken, H., 1996. “Off-Design Transition and Separation Behavior of a CDA Cascade”. *J. Turbomach.*, **118**(2), apr, pp. 204–210.
- [2] Lardeau, S., Leschziner, M., and Zaki, T., 2011. “Large Eddy Simulation of Transitional Separated Flow over a Flat Plate and a Compressor Blade”. *Flow Turbul. Combust.*, **88**(1-2), jul, pp. 19–44.
- [3] Scillitoe, A. D., Tucker, P. G., and Adami, P., 2016. “Numerical Investigation of Three-Dimensional Separation in an Axial Flow Compressor: The Influence of Freestream Turbulence Intensity and Endwall Boundary Layer State”. *J. Turbomach.*, **139**(2), oct, pp. 021011 1–10.
- [4] Adamczyk, J. J., Hansen, J. L., and Prahst, P. S., 2007. “A Post Test Analysis of a High-Speed Two-Stage Axial Flow Compressor”. In Proc. of ASME Turbo Expo 2007, ASME, pp. 377–388.
- [5] Zaki, T. A., Wissink, J. G., Rodi, W., and Durbin, P. A., 2010. “Direct numerical simulations of transition in a compressor cascade: the influence of free-stream turbulence”. *J. Fluid Mech.*, **665**, oct, pp. 57–98.
- [6] Menter, F. R., Langtry, R., Völker, S., Langtry, R., and Völker, S., 2006. “Transition Modelling for General Purpose CFD Codes”. *Flow Turbul. Combust.*, **77**(77), pp. 277–303.
- [7] Leggett, J., Sandberg, R., Priebe, S., and Richardson, E., 2017. “Loss prediction in an axial compressor cascade at off-design incidences with free stream disturbances”. In Proc. of ASME Turbo Expo 2017.
- [8] Medic, G., Zhang, V., Wang, G., Joo, J., and Sharma, O. P., 2016. “Prediction of Transition and Losses in Compressor Cascades Using Large-Eddy Simulation”. *J. Turbomach.*, **138**(12), jun, pp. 121001 1–9.
- [9] Gao, F., Zambonini, G., Boudet, J., Ottavy, X., Lu, L., and Shao, L., 2015. “Unsteady behavior of corner separation in a compressor cascade: Large eddy simulation and experimental study”. *Proc. Inst. Mech. Eng. A J. Power Energy*, **229**(5), jul, pp. 508–519.
- [10] Gbadebo, S. A., 2003. “Three-Dimensional Separations in Compressors”. PhD thesis, University of Cambridge.
- [11] Hilgenfeld, L., and Pfitzner, M., 2004. “Unsteady Boundary Layer Development Due to Wake Passing Effects on a Highly Loaded Linear Compressor Cascade”. *J. Turbomach.*, **126**(4), pp. 493–500.
- [12] Lieblein, S., Schwenk, F. C., and Broderick, R. L., 1953. Diffusion factor for estimating losses and limiting blade loadings in axial-flow-compressor blade elements. Tech. rep., NACA Research Memorandum.
- [13] Piomelli, U., and Chasnov, R., 1996. “Large-Eddy Simulations: Theory and Applications”. *Turbulence and Transition Modelling*, **2**, pp. 2269–336.
- [14] Crumpton, P., Moinier, P., and Giles, M., 1997. “An unstructured algorithm for high Reynolds number flows on highly stretched grids”. *Numerical methods for laminar and turbulent flow*, pp. 1–13.
- [15] Cui, J., Nagabhushana Rao, V., and Tucker, P., 2015. “Numerical Investigation of Contrasting Flow Physics in Different Zones of a High-Lift Low-Pressure Turbine Blade”. *J. Turbomach.*, **138**(1), oct, pp. 011003 1–10.
- [16] Rogers, S. E., Kwak, D., and Kiris, C., 1991. “Steady and unsteady solutions of the incompressible Navier-Stokes equations”. *AIAA Journal*, **29**(4), apr, pp. 603–610.
- [17] Roe, P., 1986. “Characteristic-Based Schemes for the Euler Equations”. *Annu. Rev. Fluid Mech.*, **18**(1), jan, pp. 337–365.
- [18] Tajallipour, N., Babaee Owlam, B., and Paraschivoiu, M., 2009. “Self-Adaptive Upwinding for Large Eddy Simulation of Turbulent Flows on Unstructured Elements”. *J. Aircraft*, **46**(3), may, pp. 915–926.
- [19] Bassenne, M., Urzay, J., Park, G. I., and Moin, P., 2016. “Constant-energetics physical-space forcing methods for improved convergence to homogeneous-isotropic turbulence with application to particle-laden flows”. *Phys. Fluids*, **28**(3), pp. 035114 1–16.
- [20] Smagorinsky, J., 1963. “General circulation experiments with the primitive equations”. *Monthly Weather Review*, **91**(3), mar, pp. 99–164.
- [21] Schumann, U., 1975. “Subgrid scale model for finite difference simulations of turbulent flows in plane channels and annuli”. *J. Comput. Phys.*, **18**(4), pp. 376–404.
- [22] Nicoud, F., and Ducros, F., 1999. “Subgrid-Scale Stress Modelling Based on the Square of the Velocity Gradient Tensor”. *Flow Turbul. Combust.*, **62**(3), pp. 183–200.

- [23] Nicoud, F., Toda, H. B., Cabrit, O., Bose, S., and Lee, J., 2011. “Using singular values to build a subgrid-scale model for large eddy simulations”. *Phys. Fluids*, **23**(8), pp. 085106 1–35.
- [24] Saad, T., Cline, D., Stoll, R., and Sutherland, J. C., 2016. “Scalable Tools for Generating Synthetic Isotropic Turbulence with Arbitrary Spectra”. *AIAA Journal*, **2016-03-J0**, pp. 1–14.
- [25] Bailly, C., and Juve, D., 1999. “A stochastic approach to compute subsonic noise using linearized Euler’s equations”. In 5th AIAA/CEAS Aeroacoustics Conference and Exhibit, American Institute of Aeronautics and Astronautics.
- [26] Wu, X., Jacobs, R. G., Hunt, J. C. R., and Durbin, P. A., 1999. “Simulation of boundary layer transition induced by periodically passing wakes”. *J. Fluid Mech.*, **398**, nov, pp. 109–153.
- [27] Saric, W. S., 1994. “Gortler Vortices”. *Annu. Rev. Fluid Mech.*, **26**, pp. 379–409.
- [28] Jacobs, R. G., and Durbin, P. A., 2001. “Simulations of bypass transition”. *J. Fluid Mech.*, **428**, feb, pp. 185–212.
- [29] Zaki, T. A., and Durbin, P. A., 2006. “Continuous mode transition and the effects of pressure gradient”. *J. Fluid Mech.*, **563**(2006), pp. 357–388.
- [30] Coull, J. D., and Hodson, H. P., 2011. “Unsteady boundary-layer transition in low-pressure turbines”. *J. Fluid Mech.*, **681**, aug, pp. 370–410.
- [31] Cumpsty, N. A., Dong, Y., and Li, Y. S., 1995. “Compressor Blade Boundary Layers in the Presence of Wakes”. In ASME 1995 International Gas Turbine and Aeroengine Congress and Exposition, ASME, pp. 1–16.
- [32] Sayadi, T., and Moin, P., 2012. “Large eddy simulation of controlled transition to turbulence”. *Phys. Fluids*, **24**(11), pp. 114103 1–17.